PURPOSE-LED
PUBLISHING™

PAPER • OPEN ACCESS

The suppression of anomalous impurity transport above a critical normalized density gradient scale length in Wendelstein 7-X

View the article online for updates and enhancements.

The suppression of anomalous impurity transport above a critical normalized density gradient scale length in Wendelstein 7-X

T Romba[*] , **F Reimold, S Bannmann** , **T Bleher, O P Ford,**
P Zs Poloskei , **M Wappl** **and the W7-X Team**[1]

Max Planck Institute for Plasma Physics, 17491 Greifswald, Germany

E-mail: thilo.romba@ipp.mpg.de

CrossMark

Abstract

In purely neutral-beam-heated scenarios in Wendelstein 7-X (W7-X), central peaking of impurity density profiles is observed. These are discharges typically considered as the main path towards high energy confinement in W7-X. Understanding the undesirable impurity peaking in this kind of discharge is thus paramount. In previous work, the transport in the impurity channel in this kind of discharge was found to be dominated by neoclassical and classical transport, implying a suppression of the anomalous transport component (Romba *et al* 2023 *Nucl. Fusion* **63** 076023). This paper investigates dependencies of the impurity peaking on potential drivers of changes in the impurity transport channel. Based on a vast data set, peaking of impurity density profiles is found to be stronger for higher-charge species, scaling approximately linearly with impurity charge for low Z impurities. This scaling of the peaking strength is reproduced in 1D transport simulations, which are found to match with predictions of neoclassical and classical transport inside half radius. With the match present over a wide range in plasma profiles and impurity charge, a suppression of the anomalous transport component for species helium, carbon, and oxygen is inferred. This suppression of anomalous transport is not found to strongly depend on the magnetic field configuration, rendering it a more general W7-X feature. A critical normalized electron density gradient scale length $a/L_{n_e} \approx 1.0$ is identified as a parameter indicative to the change in anomalous impurity transport. For these particular

experimental scenarios, the appearance of this critical scale length is found to be coupled to a high plasma density. The critical value of a/L_{n_e} is found to only be applicable in regions of peaked impurity density profiles, indicating a radial dependency.

Keywords: Wendelstein 7-X, stellarator, impurity transport

1. Introduction

While impurities were observed to potentially improve the performance of fusion-relevant plasmas [1, 2], in view of sustained burn in a fusion reactor, their foremost effect lies in restricting the feasible operating range [3]. To mitigate their restricting effects, impurity transport needs to be understood in current day devices in order to tailor it to acceptable level, shape, and sign in future machine designs. While concentrations of several percents for the fusion ash helium are anticipated and tolerable [4], allowable concentrations of high Z impurities are significantly lower (concentrations around 1×10^{-4}) [3]. These values demand for a sufficiently high outward directed transport of helium in combination with a good edge screening of higher Z impurities.

The transport of energy, particles, as well as impurities is governed by the sum of the classical, neoclassical, and anomalous transport components. While classical transport is small under fusion conditions [5], neoclassical transport is large in non-optimized magnetic field geometries [6]. Due to the strong scaling of the latter with impurity charge Z, it is most important for high Z impurities such as tungsten. Anomalous transport describes the joint transport from turbulent as well as other transport processes and is so-far less understood in stellarator devices.

The Wendelstein 7-X stellarator (W7-X) [7, 8] was optimized for and has successfully shown to exhibit low neoclassical energy transport [9]. Typical W7-X plasmas are heated by electron cyclotron resonance heating (ECRH). Under these conditions, profiles of low to medium Z impurities are found to be flat [10]. In line with experimental and theoretical predictions for iron [11], their transport is dominated by a diffusive anomalous component [10]. Transport of high Z impurities is found to be independent of impurity charge [12, 13], with transport of iron at low density being dominated by a diffusive anomalous transport component [14].

Besides these scenarios with energy confinement times well below the ISS04 [15] scaling predictions, other W7-X scenarios with improved confinement characteristics were identified [16–20]. In two of these scenarios, plasmas purely heated by neutral-beam-injection (NBI) [18] and ECRH plasmas at low power and density [19], a reduction of low to medium Z impurity transport to (neo)classical levels was identified [18, 19]. Here, (neo)classical relates to the sum of classical and neoclassical transport.

With the purely neutral-beam-heated scenario being used to achieve high energy confinement in W7-X [21], the impurity transport in these conditions is a central puzzle piece in

assessing overall performance and reactor compatibility. As the current discharge parameters lead to unacceptable impurity concentrations, impurity transport in those scenarios needs to be understood and subsequently tailored in order to reach reactor-relevant levels.

As the impurity content is set by the transport in the impurity channel, actuators of this are expected to alter the central impurity density, potentially so much that scenarios of reduced impurity content can be identified. Besides changes in trapped particle population in the form of collisionality variations, changes in the degree of quasi-isodynamicity by means of changes in the magnetic field topology constitute potential actuators investigated here.

This paper will assess impurity transport in purely NBI-heated discharges as previously discussed in [18], aiming to identify dependencies on actuators of the impurity transport. The methodology is introduced in section 2 with the experimental scenario studied being introduced in section 3. Dependencies of impurity density peaking on plasma density, magnetic configuration, and impurity charge are reported in section 4. A comparison between 1D transport modeling and measurements is performed in section 5. The work concludes with an assessment of the data in form of a database approach in section 6 and summarizes in section 7.

2. Methodology

2.1. Transport of impurities

Impurities in a fusion reactor are either sourced in the plasma core (He) or outside the confined region (C, W, seeding gases). From these local sources, impurities are spatially distributed by transport processes. The change in local impurity density n_z can be described using a diffusive-convective approach parametrizing the impurity flux Γ_z. Including a local source S_z, the transport of the impurity charge state Z is described by:

$$\frac{\partial n_z}{\partial t} = -\nabla \Gamma_z + S_z = -\nabla (V n_z - D \nabla n_z) + S_z, \quad (1)$$

where D and V are the diffusion and convection coefficients acting on the impurity of charge Z. In this parametrization, transport contributions from the different transport mechanisms are summed into joint coefficients.

Under W7-X conditions, low Z impurities are found to be fully ionized throughout most of the plasma [10]. In such regions, the source term in equation (1) vanishes. With temporally and spatially resolved densities of the fully ionized

charge state obtained from measurements, the diffusion and convection coefficients constitute the sole unknown parameters of equation (1). The plasma regions relevant in the following are found to all exhibit sufficiently high T_e to meet this condition.

To parameterize the local profile shape of the impurity density in the following, the normalized impurity density gradient scale length, a/L_{n_z}, is used. This is defined as:

$$a/L_{n_z} = -a\frac{\langle \nabla n_z \rangle}{n_z} = -\frac{a}{n_z}\frac{\partial n_z}{\partial \rho}\langle \nabla \rho \rangle, \qquad (2)$$

where ρ denotes the normalized minor radius and a is the configuration-dependent, minor radius of the plasma. Flux surface averages are indicated by $\langle \rangle$ with $\nabla \rho$ denoting a geometrical factor accounting for the three-dimensional geometry of W7-X. Normalized scale lengths for other parameters are defined equivalent to equation (2).

This parameter refers back to the transport properties of the plasma as it is equivalent to the steady state solution of the source free transport equation (1) with $a/L_{n_z} = -aV/D$. In this limit, a/L_{n_z} characterizes the relative strength of the convective and diffusive transport component, thus the steepness of the impurity density profile.

2.2. Impurity density measurements

In order to derive the local impurity transport properties from equation (1), profile information on the assessed species needs to be obtained. For impurities, charge exchange recombination spectroscopy (CXRS) [22] allows for the necessary localized impurity density measurements.

In the following, impurity emission is measured with the W7-X CXRS system [23] and analysed following the scheme described in [10]. The Monte-Carlo code pyFIDASIM [24] is replaced by a fully collisional-radiative and deterministic beam model employing a diffusive approach to model the beam halo [25], allowing for a significant speedup in computational time.

3. Scenario

An overview of a typical experimental scenario is given in figure 1. To establish a reference plasma for take over by NBI, 3 s of ECR heating at fixed density set point is used. The stabilized plasma is then taken over by two neutral beam sources with a total of 4 MW of neutralized power.

During the ECRH phase, a density set point (dashed horizontal line in central plot) is established and maintained. Upon the switch to NBI heating [26], both, the line integrated as well as on-axis, density increase above the unchanged density set point.

During the NBI phase, electron and ion temperatures equilibrate. This arises from the comparable NBI power coupled to the two species in combination with the high collisionality. Starting from 1.3 keV, on-axis temperatures are found to
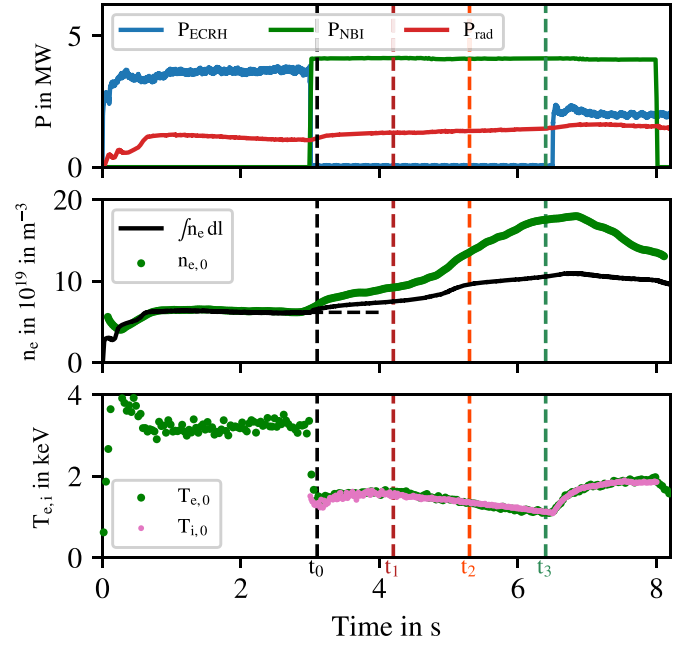
Figure 1. Overview of W7-X discharge 20230316.066. Vertical lines indicate time stamps of the profiles of figure 2. The experiment is conducted in the low mirror magnetic configuration of W7-X.

initially increase to values up to 1.5 keV. Afterwards, they decrease to values around 1 keV as the density increases, attributed to the decrease in power per particle.

Starting at 6.5 s, ECRH is reintroduced into the high density plasma. As a consequence, temperatures are found to increase, in turn increasing the stored diamagnetic energy. Ion temperatures are found to exceed the clamping limit of 1.6 keV [27].

The equilibration of ion and electron temperature causes the ion mobility to exceed that of the electrons. This gives rise to ion-root confinement with an inward-directed negative radial electric field throughout the whole plasma in phases of $T_e \approx T_i$.

Radial profiles of the electron and C^{6+} density at four points in time during the pure NBI phase are depicted in figure 2. Density measurements of the electrons are performed with Thomson scattering [28], impurity ones with CXRS.

While profiles of electron and C^{6+} density are initially parabolic and flat, respectively, both peak with time after the transition to pure NBI. In the carbon case, this peaking is limited to $\rho \leqslant 0.5$ while peaking of the electron profile is found to be broader with $\rho \leqslant 0.7$. Note that due to the stronger increase in carbon than electron density, the central impurity concentration increases with time.

The dominant transport mechanisms for electrons and impurities in the scenario at hand was assessed in previous publications [18, 20]. In [20], it was shown that the anomalous component of the main particle transport is found to reduce upon the onset of density peaking. The anomalous flux component in the electron channel remains however significant. The central peaking in electron density was found not to be a beam fueling effect but requires a change in main species
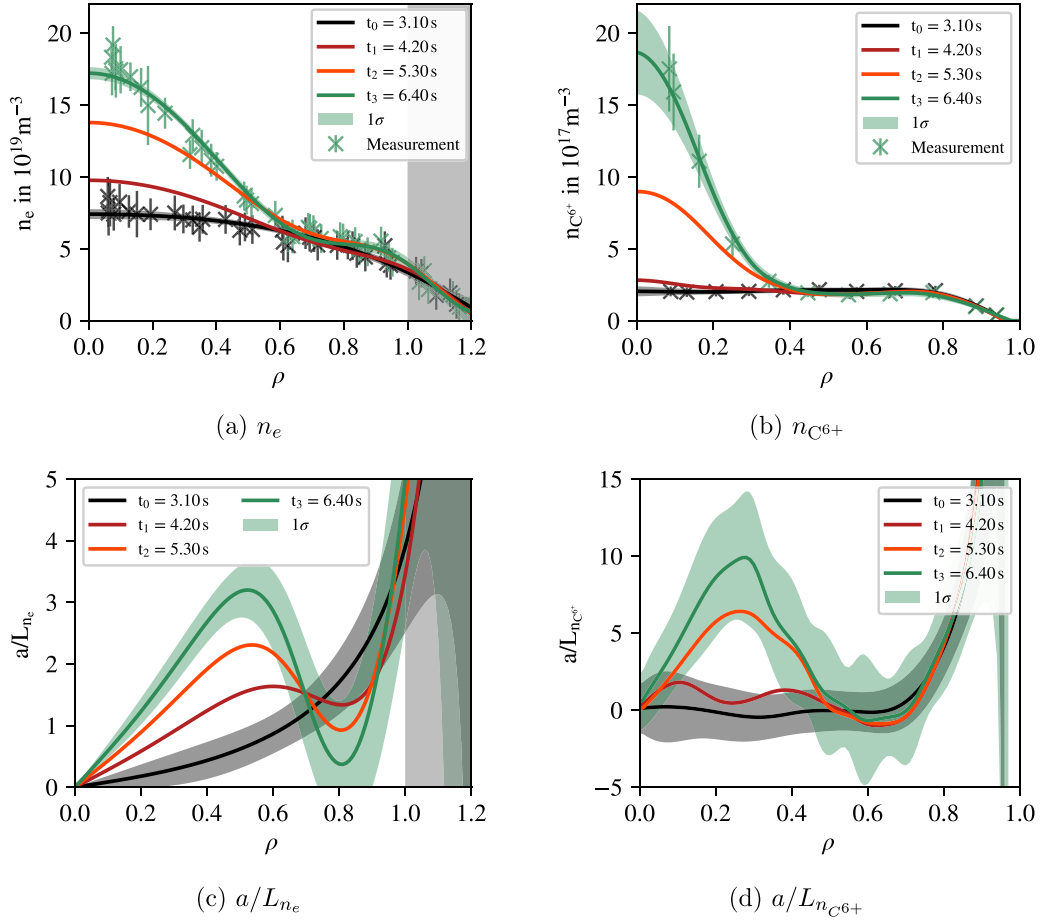
Figure 2. Profiles of electron and C^{6+} density and their normalized density gradients scale length for four time points of W7-X discharge 20230316.066. Underlying measurements from Thomson scattering (n_e) and CXRS ($n_{C^{6+}}$) are shown for two time instances. The non-confinement region ($\rho > 1.0$) is shaded.

transport with increased V/D [20]. In contrast, for the impurities it was shown in [18] that the profile evolution of C^{6+} and Ar^{16+} can be matched when assuming (neo)classical transport only, implying a suppression of the anomalous transport component in the impurity channel.

As the ion temperature is found to exceed the clamping limit set by ITG turbulence [27], a change in energy transport accompanying the change in main ion and impurity transport has to be present. Note that this change in energy transport is expected not to be limited to the phase of joint NBI and ECRH but rather not to be evident in the earlier phase due to the low heating power. Exceeding the ion temperature clamping limit renders the scenario relevant as it constitutes a path towards higher ion temperature in W7-X.

Note that the increase in density in combination with the strongly coupled temperatures causes the scenario to be self-similar for various parameters. This in turn makes variations in certain parameters impossible (e.g. T_e/T_i) or does not allow for a controlled scan in others (e.g. η_i, a/L_{n_e}). In contrast to the inability to assess dependencies on the above parameters, the strong variation in impurity density gradient might allow the assessment of the influence of impurity density gradients on turbulent transport. Here, recent advances in turbulence modeling predict a strong modification of turbulent heat fluxes by impurity density gradients [29].

3.1. Impurity peaking proxy

In the context of figure 2, a significant change in shape of the impurity density profiles from flat to strongly peaked was introduced. While local parameters are the drivers for the underlying transport phenomena, an indication of a change in transport can already be obtained from coarser, yet easier to assess, parameters.

As a figure of merit for the peaking of the impurity density profile, the ratio of two charge exchange measurements is used in the following. By choosing one measurement location close to the magnetic axis (ρ_1) and one outside the region of impurity density peaking (ρ_2), the ratio $n_z(\rho_1)/n_z(\rho_2)$ constitutes a proxy for the steepness of the impurity density profile and will be referred to as the peaking factor in the following. In the case of flat impurity density profiles, this peaking factor equates to unity as the densities in both locations are equal. For peaked impurity density profiles, $n_z(\rho_1)$ is increased while
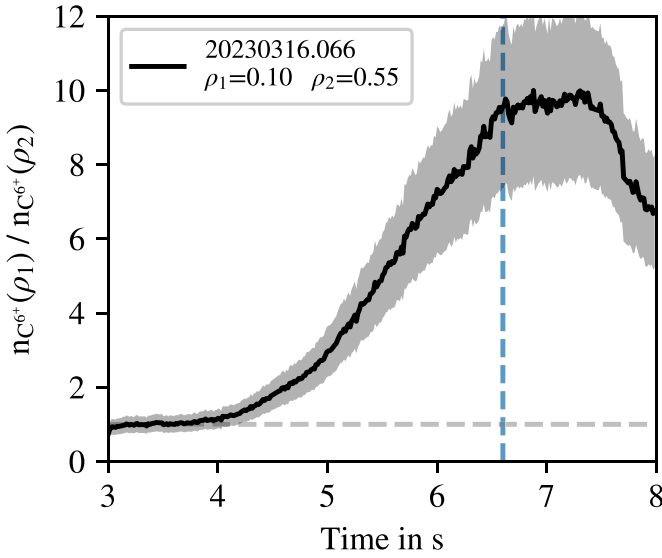
Figure 3. Impurity profile peaking factor for C^{6+} in the case of W7-X discharge 20230316.066. 2MW of ECRH is reintroduced starting at the blue dashed line.

Figure 4. Time traces of the line integrated densities for the performed density scan. Density set points are indicated by dashed horizontal lines. Plasmas are established by ECRH with heating powers of 3, 2, and 2 MW in discharges 041, 047, and 051, respectively. The dashed vertical line indicates the switch from ECRH to NBI heating with 4.0 MW from two neutral beam sources. Experiments are conducted in the high mirror magnetic configuration of W7-X.

the density at ρ_2 remains approximately constant, causing the peaking factor to increase with central peaking of the impurity density.

Due to changes in the magnetic configuration as well as the underlying plasma equilibria, the precise location of the chosen channels varies between and within experiments. While changes within an experiment due to Shafranov shifts are small due to the low stored plasma energy, differences between magnetic configurations are substantial. To enable a comparability nonetheless, measurements assessing different magnetic configurations are chosen to match in ρ_1 and ρ_2.
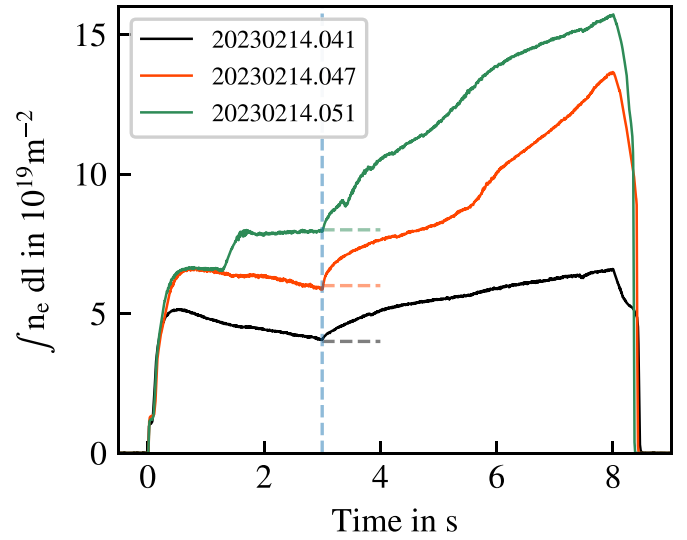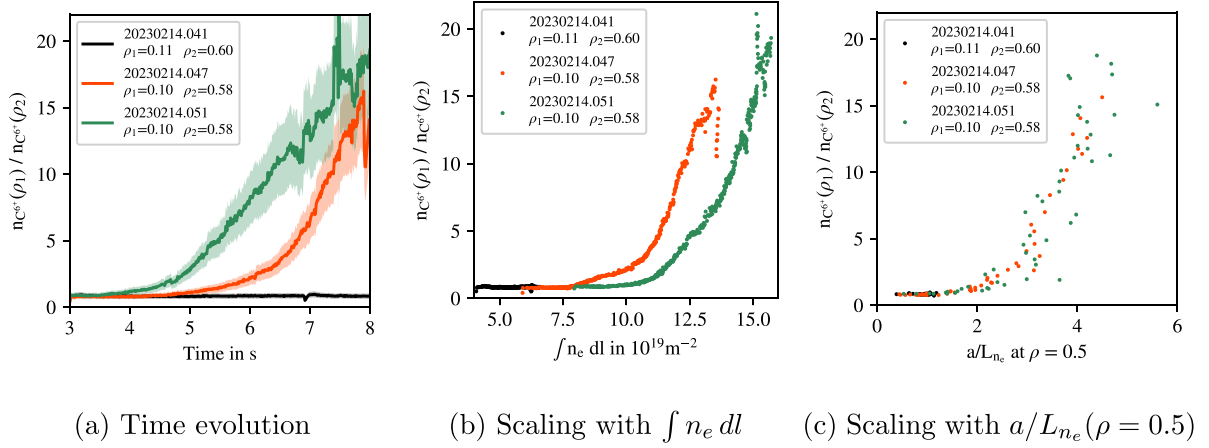
The time evolution of the peaking factor in the case of the paradigmatic discharge of figure 1 is given in figure 3. While it initially lies around unity, corresponding to flat impurity density profiles, latter profiles are found to exhibit a high peaking factor, consistent with the profile evolution of figure 2(b). With the peaking factor matching the expectations, it constitutes a suited parameter to assess the impurity density profile shape in the following.

4. Impurity transport dependencies

4.1. Density dependence

Plasma density influences transport processes either via collisions that affect both the neoclassical transport and the turbulent transport through collisional detrapping or via the density gradient, which affects the turbulent drive. With the uncontrolled increase in density observed in the scenarios assessed herein, a dependence of the assessed scenario on density arises as a natural question.

Figure 2(a) showed an overall increase in electron density in form of more and more centrally peaked electron density profiles over the course of the discharge. In contrast, electron density profiles in similar discharges at lower density are found to increase in total density as well, but profiles retain the parabolic shape of t_1 of figure 2(a). These parabolic profiles are found to be self-similar up to a certain high density above which the central peaking in the electron density profile onsets (compare figure 2). Impurity density profiles are found to remain flat in the case of parabolic n_e profiles and to only peak in cases of centrally peaked ones.

This self-similarity of the electron density profiles for low to medium densities in combination with an increase in density during the NBI phase allows for a continuous scan in density up to the onset of the peaking in the electron density profile. Monitoring the response of the impurity density profiles in such a scan in turn allows to assess dependencies of the studied impurity peaking on the total electron density and its profile shape.

Measured line-integrated densities for three W7-X discharges constituting such a scan are given in figure 4. The scan is split up into three discharges as NBI operation in W7-X is limited to 5 s. The applied heating scheme is equivalent to figure 1 with takeover of an ECRH plasma by two neutral beam sources at a program-specific density value. The heating powers in the ECRH phase vary slightly (3, 2, and 2 MW), have no effect on the NBI phase due to the fast equilibration of the electron and ion temperatures, however (compare figure 1).

The densities are found to increase above the density set point (dashed lines) in all three cases upon the switch to NBI heating at 3 s. While an increase is present across all scenarios, a significant difference in the rate of change is present. The line-integrated density is found to increase the slowest in the

(a) Time evolution $\quad$ (b) Scaling with $\int n_e \, dl$ $\quad$ (c) Scaling with $a/L_{n_e}(\rho = 0.5)$

Figure 5. Peaking factor for C^{6+} in the case of the density scan of figure 4.

case of the low density discharge, while for the higher-density discharges the density increases more rapidly.

The time evolution of the peaking factor of C^{6+} in the case of the three conducted experiments is displayed in figure 5(a). Carbon profiles in the low-density discharge are found to be slightly hollow, with a peaking factor of around 0.8. After an initial phase of similar carbon density profiles, the higher density discharges are found to exhibit strongly peaked profiles (peaking factor $\gg$ unity). The peaking factor reaches up to 20 toward the end of the higher density discharges.

Figure 5(b) depicts the dependence of the peaking factor of carbon on the line integrated electron density. It is found that peaked impurity density profiles only occur for line integrated densities above $8 \times 10^{19} \, \text{m}^{-2}$. This connects the central peaking of the impurity density profile to a high density. Note that this observation may only be valid for the plasma scenario in use, i.e. takeover of an established reference plasma of 3 MW of ECRH by NBI.

While a central peaking of impurity density is found to only occur at high line-integrated density, the data of figure 5(b) indicates no unique scaling of the peaking factor with line-integrated density. In contrast, a unique scaling of the peaking factor is obtained when plotted against a/L_{n_e} at $\rho = 0.5$, depicted in figure 5(c). With this location lying in between the two reference points used to determine the peaking factor, this parameter can be interpreted as a characteristic normalized gradient scale length of the main density profile. With a/L_{n_e} being linked to a/L_{n_i} via the quasi-neutrality condition and simulations of turbulent transport in W7-X predicting a reduction in turbulence by an ion density gradient [30], a reaction of turbulent transport to a/L_{n_e} is anticipated.

The combination of the previous, potentially scenario-specific, observations indicates the intrinsic formation of a strong absolute electron-density gradient, developed at high density only. This leads to the conclusion that a central peaking of impurity density profiles in the case of the scenario at hand only develops for $a/L_{n_e}(\rho = 0.5) \geqslant 1.0$, a parameter range only reached at high line integrated density. The role of the impurities on the dilution of the main ions, and thus

Table 1. Effective helical ripple (ε_{eff}), trapped particle fraction (f_{tr}), and an ITG turbulence proxy (f_{ITG}) of the magnetic configurations assessed.

| Configuration	$\varepsilon_{\text{eff}, \rho=0}$	$\varepsilon_{\text{eff}, \rho=0.5}$	$f_{\text{tr}, \rho=0}$	$f_{\text{tr}, \rho=0.5}$	f_{ITG} [31]
Low mirror (AIM)	0.0071	0.0152	0.174	0.344	9.3
Standard (EIM)	0.0066	0.0060	0.293	0.430	10.1
High mirror (KJM)	0.0241	0.0224	0.454	0.542	11.2

a distinction between the normalized density gradient scale length of the electrons (a/L_{n_e}) and ions (a/L_{n_i}), is not assessed in the following and envisioned for future work. Note that further, gyrokinetic modeling predicts a significant modification of turbulent transport in the presence of impurity density gradients [29].

4.2. Magnetic configuration dependence

The shape of trapped-particle orbits plays a key role in setting the transport properties of a plasma. As these orbits are set by the magnetic-field geometry, the variability in the magnetic field of W7-X allows assessing influences of such on impurity transport properties.

In order to probe the reaction of the impurity transport to a change in magnetic topology of W7-X, similar experiments were performed in W7-X configurations of changing magnetic mirror ratio. The three assessed configurations are the low mirror (W7-X three-letter code AIM), standard (EIM), and high mirror (KJM) magnetic configurations. These differ in magnetic mirror ratio while keeping the main 5/5 resonance at the edge. An overview of the effective helical ripple, ε_{eff}, and the trapped particle fraction, f_{tr}, near the magnetic axis and at half radius, as well as f_{ITG} [31] are given in table 1.

ε_{eff} constitutes a figure of merit for neoclassical transport, with smaller values relating to reduced neoclassical transport. With regard to turbulent transport, linear instability theory predicts that the separation of bad curvature regions from locations of trapped particles should reduce gyrokinetic
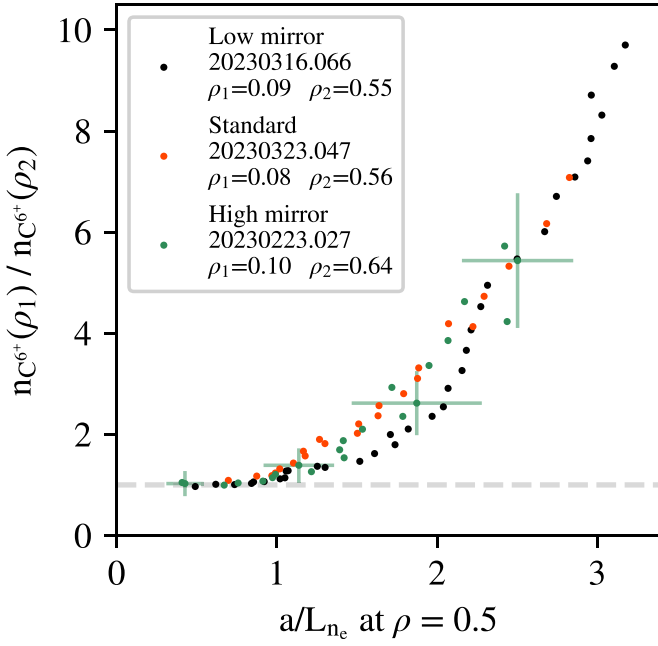
Figure 6. Impurity profile peaking factor in the carbon case versus a/L_{n_e} at $\rho = 0.5$ for W7-X configurations with changing magnetic mirror ratio.

Figure 7. Impurity densities normalized to the pre-peaking value for impurities He^{2+}, C^{6+}, and O^{8+} in the case of W7-X discharge 20230316.066. ECRH is reintroduced starting at the blue vertical line.

instabilities' growth rates [32, 33]. However, this effect could be subdominant to other changes in geometric features. One such feature is captured by f_{ITG}, constituting a measure of flux compression in bad curvature. Smaller values of f_{ITG} have been shown to correlate with reduced ITG turbulent heat flux [34].

In figure 6, the peaking factor of the carbon density profile is plotted against $a/L_{n_e}(\rho = 0.5)$ for discharges in the three assessed magnetic configurations. Error bars at four instances of the high-mirror data set are shown. In line with the observations of section 4.1, the peaking factor remains unchanged for $a/L_{n_e}(\rho = 0.5) \leqslant 1.0$ while it increases for larger values. Lower values for the peaking factor in the case of the low mirror data are observed in the $1.0 \leqslant a/l_{n_e}(\rho = 0.5) \leqslant 2.5$. This systematic offset cannot be explained by the error bars indicated as those relate to uncertainties in the profile fits. However, the deviations are expected to lie within the uncertainties of the optical geometry in combination with the localization of the diagnostic signal (discussed in more detail in section 5).

While these significant uncertainties do not allow for a detailed interpretation of the measured signals, an overall trend of strongly peaked impurity density profiles with increasing steepness of the electron density profile across the assessed magnetic configurations is apparent. In [18], measured impurity densities in the discussed kind of scenarios in the case of the high mirror magnetic configuration were shown to match transport simulations of purely (neo)classical transport. A similar exercise performed in section 5 recovers a qualitative match between measurements and transport simulations of underlying (neo)classical transport simulations in the case of the low mirror discharge of figure 6. A transport analysis assessing a match of the neoclassical transport simulations in the case of the outstanding standard configuration is subject to future work.
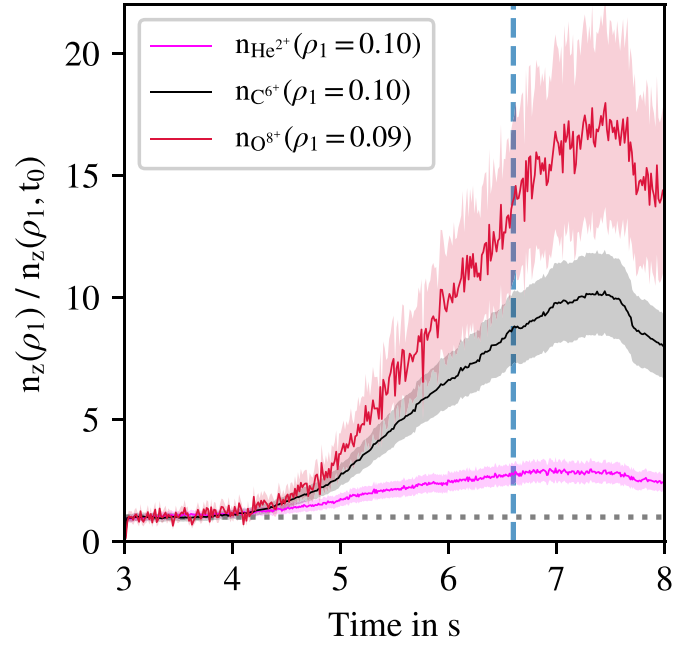
4.3. Impurity charge dependence

In regimes of small normalized temperature gradient, the convective component of the neoclassical transport scales linearly with impurity charge Z. Assessing the relative strength of the central impurity peaking for impurities of varying charge Z therefore allows for a direct comparison of experimental results with neoclassical predictions. In the case of suppressed anomalous impurity transport, a linear scaling between strength of impurity peaking and impurity charge is therefore expected.

To validate this prediction in the case of the discharge of figure 1, the time evolution of the central impurity densities for He^{2+}, C^{6+}, and O^{8+} is given in figure 7. Note that in place of the previously used peaking factor, the time evolution of $n_z(\rho_1)$ normalized to its value in the pre-peaking phase (3.1 s–3.3 s) is plotted. This is necessary due to the larger noise in the oxygen signals after boronization. The depicted data is found to be similar to the previously used peaking factor as $n_z(\rho_2)$ was found to barely change in time (compare section 3.1).

Starting at unity, the normalized densities increase for all three species with time. The density peaking is stronger the higher Z. As values are found to increase across all species at the same point in time, a global change in impurity transport characteristic affecting all assessed impurities alike must be at play.

At the point of ECRH reintroduction, normalized densities of 2.75, 8.75, and 13.5 are present for He^{2+}, C^{6+}, and O^{8+}, respectively. Normalized to the value of helium, the carbon and oxygen data show a stronger peaking by factors 3.2 ± 0.7 and 4.9 ± 1.4, respectively. While these values do not perfectly reproduce the (neo)classically predicted linear

scaling with Z (factors of 3 and 4, respectively), expectations are matched within error bars. The value in the helium case features an additional systematic error in the form of the not corrected for plume emission. This is expected to not alter the values significantly, however.

With the (neo)classically predicted scaling with Z being met by measurements, strong restrictions are put on the scaling of any competing transport channel with charge. With theoretical predictions of impurity transport in W7-X indicating no strong dependence of the turbulent convection on impurity charge [13], the observed scaling hints towards a dominant (neo)classical convection in the assessed scenario.

5. Transport modeling

With (neo)classical transport coefficients being calculable from plasma profiles, purely (neo)classical solutions of the transport equation (equation (1)) can be obtained with comparable small effort. In the case of a dominant (neo)classical transport channel, measurements and such simulations are expected to match. The combination of the previously discussed charge dependence and the wide range of plasma parameters covered within a single discharge, allows to assessed such a match over a wide range in transport relevant parameters. Identifying a potential match would impose strong restrictions on any competing transport channel, giving valuable insights into the anomalous transport in those experimental scenarios.

The (neo)classical transport coefficients necessary to perform such a comparison in the W7-X case are calculated from DKES [35] coefficients using the NEOTRANSP code [36]. However, based on the findings of [18], the so obtained transport coefficients only describe the measured impurity densities in the domain of peaked impurity density profiles. Impurity transport before the onset of impurity peaking and radially outside the peaking radius of $\rho = 0.5$ was found to be dominated by a diffusive anomalous transport component, D_{anom}.

To assess the match of (neo)classical predictions with measurements in the case of the discharge of figure 1, 1D transport simulations are performed using the pySTRAHL code [24]. Simulations are performed for He, C, and O. Across the whole domain, no anomalous convection is assumed, i.e. $V_{anom} = 0$ everywhere. Initially, D_{anom} is set to $0.3\,\mathrm{m^2\,s^{-1}}$, resulting in flat impurity density profiles. Upon the onset of impurity density peaking at 4 s, D_{anom} is reduced to $0.001\,\mathrm{m^2\,s^{-1}}$ for $\rho \leqslant 0.5$ and remains at this value for the rest of the discharge, including the phase of joint NBI and ECR heating.

Resulting local density time traces are plotted in figure 8. Simulation results are given by dashed lines, while measurements and their uncertainties are given by solid lines and shaded regions, respectively. For an improved match between measurement and simulation, measurement locations are shifted inwards by $\Delta\rho = 0.07$. This shift lies within the uncertainties of the line of sight geometry in combination with uncertainties in the location of the neutral beam. Note that this correction is of coarse character and needs to be improved by future measurements of the geometry. Due to the changing

background conditions, He^{2+} densities were not corrected for plume [37] emission. To reduce the sensitivity of the determined densities to this spectral component, helium spectra were fitted imposing the temperature determined from carbon measurements. The progressive introduction of impurity peaking reported in [18] has not been accounted for due to the uncertainties in the line of sight geometry.

Across the three impurities, the temporal behavior of the measurements is qualitatively reproduced by the transport simulations across the three radial locations displayed. After an initial phase of flat density profiles (measurements at different radii with same density), impurity density profiles peak across all species. Upon reintroduction of ECRH at 6.5 s, electron density profiles are found to become broader while maintaining a peaked shape. Coincidentally, impurity peaking is found to first stagnate and eventually decrease. The discharge terminates before impurity profiles return to their initial flat state. Note that D_{anom} remains at the suppressed value of $0.001\,\mathrm{m^2\,s^{-1}}$ also in the phase of combined NBI and ECR heating, thus (neo)classical transport predictions are found to match measurements in a phase of distinct plasma heating as well.

Note that the observed qualitative match in the ECRH + NBI heated phase is presumably limited to phases of joint ECRH and NBI heating in plasmas with a previously established density gradient. Reversed scenarios of the same joint heating powers without a previously established density gradient do not necessarily show the same behavior.

While the time evolution of some measurements is well-matched by the simulation throughout the whole discharge, others show significant deviations. These deviations are most likely due to the aforementioned uncertainties in viewing geometry combined with insufficient capability to reconstruct magnetic equilibria. With increasing peaking, the on-axis pressure increases, shifting the magnetic axis radially outwards. As the diagnostic mapping in W7-X currently relies on a precalculated set of VMEC equilibria, the mapping of diagnostic signals in scenarios of strongly changing, strongly peaked plasma pressure profiles is only coarse, introducing significant uncertainties in the measurement location.

In addition to this local mismatch between experiment and simulation, an inferior match is observed in the phase of reintroduced ECRH after 6.5 s. This minor mismatch potentially hints towards the reintroduction of a reduced anomalous transport component, which would need to remain small compared with the (neo)classical one. However, the presented uncertainties do not allow to assess this possibility with sufficient sensitivity.

Simulations are found to match the approximately linear scaling with impurity charge observed in figure 7. This indicates the applicability of (neo)classical transport not only to the significant range in plasma parameters covered during the peaking and ECRH reintroduction phases, but further to a significant range in impurity charge. Note that in contrast to this charge dependence correctly described by (neo)classical transport, experimental investigations in regimes of dominant anomalous transport showed no charge dependence of the impurity confinement time in W7-X [12].

(a) He^{2+} (b) C^{6+} (c) O^{8+}
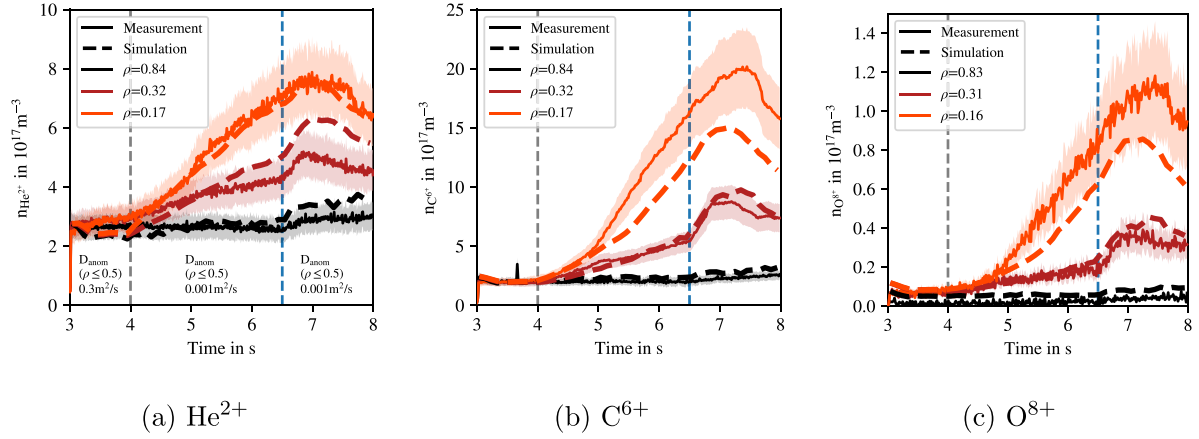
Figure 8. Comparison of time traces from pySTRAHL (dashed lines) and the experiment (solid lines with shaded error regions) at different radial locations in the case of the experiment of figure 1. Starting with the gray vertical line at $t = 4\,$s, imposed transport is reduced to (neo)classical levels for $\rho \leqslant 0.50$. ECRH is reintroduced starting with the blue vertical line.

The compatibility of measurements with (neo)classical expectations not only in charge dependence (compare section 4.3) but over a wide range of plasma parameters puts strong restrictions on the scaling of any competing transport channel. With impurity transport in ITG-dominated regimes of W7-X found to be charge-independent, a suppression of the anomalous transport component for impurities He^{2+}, C^{6+}, and O^{8+} is the most logical explanation of the measurements.

6. Database

While the modeling of impurity transport in selected cases can give information on changes in the dominant impurity transport channel, potential drivers for this change cannot be deduced. To identify drivers of the suppression of the anomalous impurity transport, a database approach collecting data across similar discharges is used. By identifying parameters at which a transition from dominant anomalous to dominant (neo)classical transport takes place, insights into the dependencies of the underlying instabilities may be obtained.

With turbulent transport being driven by instabilities, changes in local gradients are the prime candidates for potential causes for the suppression of anomalous impurity transport. Figure 9 displays an overview of the dependence of the normalized density gradient scale length of carbon, $a/L_{n_{C6+}}$, on the normalized gradient scale lengths of electron density, electron temperature, and ion temperature at $\rho = 0.2$. Due to the difficulties in the localization of the OP2.1 data discussed in section 5, data is restricted to that of OP1.2b of 2018 in the following, as localization uncertainties are smaller there. In this limited data set, only phases of pure NBI heating have been accounted for, with all experiments being conducted in the high mirror (KJM) magnetic configuration. Note that, due to the evolving nature of the scenario, the depicted values do not constitute steady-state parameters.

In accordance with the observations of section 4, a/L_{n_e} is found to order the measured $a/L_{n_{C6+}}$ well. Again, a separation into two groups is present, one with $a/L_{n_{imp}} \approx 0$ (approximately equivalent to a peaking factor of unity) and one with finite $a/L_{n_{C6+}}$ (approximately equivalent to the peaking factor exceeding unity). The two groups are found to separate at $a/L_{n_e} \approx 1$. Note that the separation between the two groups is more distinct than in section 4 due to the assessment of local properties in contrast to the previously used proxies assessing whole regions of the impurity density profile.

Even though the normalized gradients scale lengths of both, ion and electron temperature, a/L_{T_i} and a/L_{T_e}, are expected to have a strong influence on the turbulence-driving instabilities, no unique scaling of $a/L_{n_{C6+}}$ with them is apparent. The decrease of a/L_{T_e} and a/L_{T_i} with increasing $a/L_{n_{C6+}}$ can be attributed to the simultaneous increase in line-integrated density and impurity peaking. Due to the increase in the total number of particles, the power per particle is reduced, resulting in an overall drop of temperatures and subsequently their gradients. A further disentanglement of these parameters is challenging due to the low level of control of the assessed scenario.

As the impurity peaking is radially limited to $\rho \leqslant 0.5$, a dependence of the change in transport on radius is apparent. To probe this, figure 10 depicts $a/L_{n_{C6+}}$ plotted against a/L_{n_e} at different radii. Finite impurity density gradients are observed only to occur inside the peaking radius. Radially further outwards, a/L_{n_e} strongly exceeds the value of unity with no impurity density gradient being present. This reduces a critical a/L_{n_e} of unity to a necessary condition, indicating that other, radially dependent, effects such as the plasma collisionality play an important role in setting the impurity transport.

The observed dependence of the anomalous transport channel on a/L_{n_e} is in line with a stabilization of ITG turbulence by a density gradient [38, 39]. In line with the above findings for the impurity transport channel, the transition in main particle transport was identified to occur at similar normalized

(a) $a/L_{n_{C6+}}$ vs a/L_{n_e} (b) $a/L_{n_{C6+}}$ vs a/L_{T_e} (c) $a/L_{n_{C6+}}$ vs a/L_{T_i}
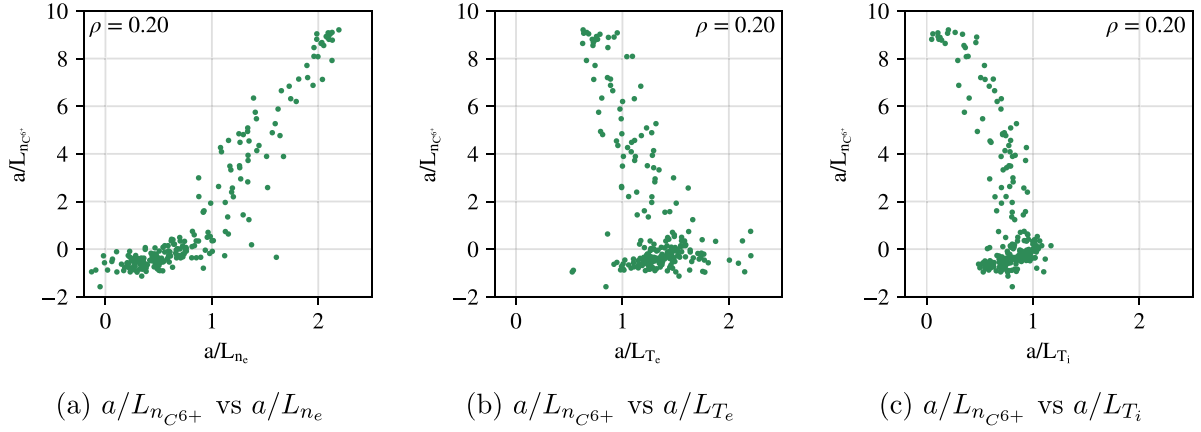
Figure 9. Normalized impurity density gradient scale length versus normalized gradient scale lengths of the main plasma parameters at $\rho = 0.2$. Experiments are conducted in the high mirror magnetic configuration.

(a) $\rho = 0.15$ (b) $\rho = 0.2$ (c) $\rho = 0.3$

(d) $\rho = 0.35$ (e) $\rho = 0.4$ (f) $\rho = 0.5$
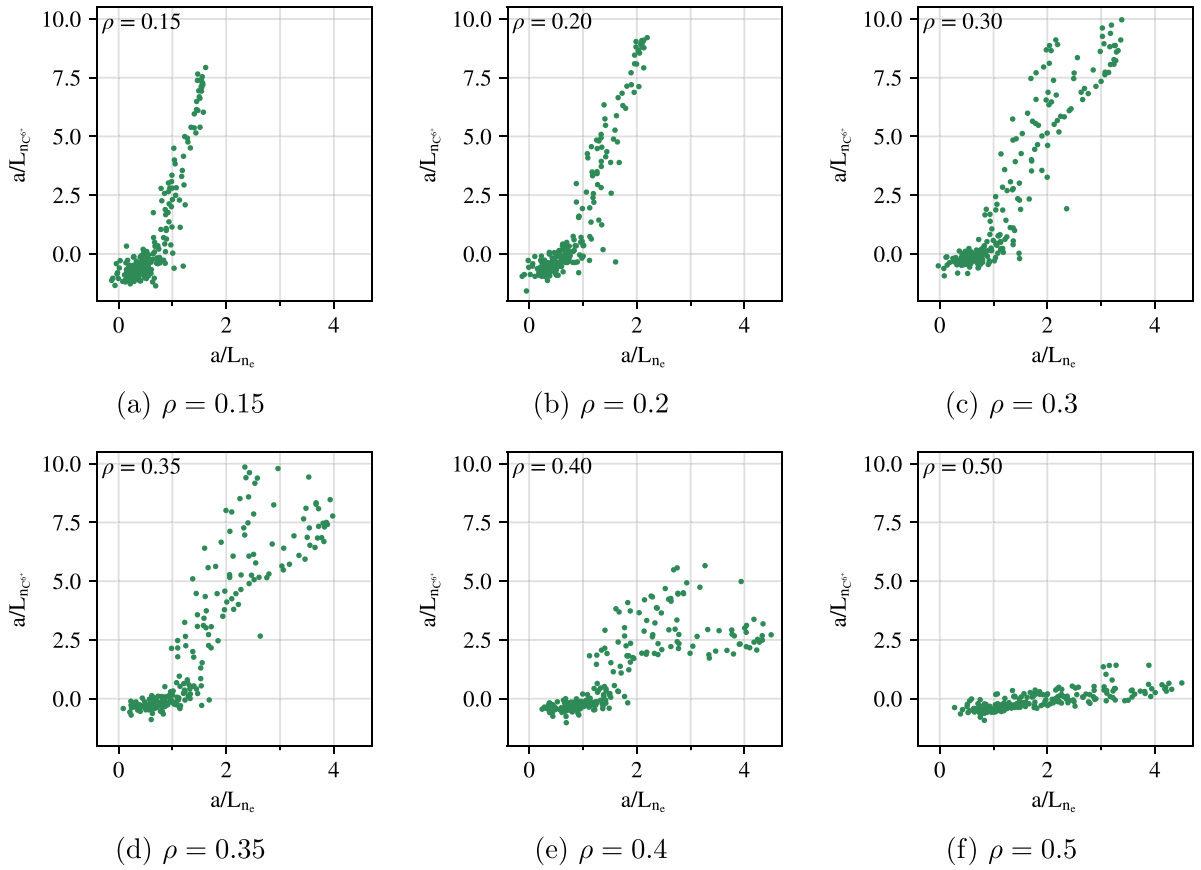
Figure 10. $a/L_{n_{C6+}}$ vs a/L_{n_e} at different radii.

electron density gradients [20]. While the above identification of a threshold value indicates a significant dependence on a/L_{n_e}, further probing the available parameter space is central to obtaining a deeper insight into the transport dependencies of W7-X. Changes in magnetic field strength alter the Larmor radius, affecting the classical and neoclassical transport channels via a change in characteristic step size and turbulent transport via changes in the gyro Bohm scaling factor. Varying the number of neutral beam sources alters the power per particle, potentially exceeding the ion temperature clamping limit in phases of pure NBI operation. Such investigations are subject to current experiments and will be assessed in future publications.

7. Summary

Transport of impurities in purely NBI heated W7-X plasmas has been analyzed with respect to parameters relevant to changes in the dominant impurity transport channel. In line

with previous findings, centrally peaked impurity density profiles for elements helium, carbon, and oxygen were found to be matched by purely (neo)classical transport in profile shape as well as time evolution. Due to the observed match between (neo)classical predictions and experiments over a wide parameter range, a suppression of the competing anomalous transport component is inferred.

Based on an extended data set, this suppression of anomalous transport is found to occur for different magnetic configurations, rendering it a more general feature of W7-X, present at high collisionality. In the case of the imposed experimental scenario, a high density was identified to be necessary for central peaking of impurity density profiles to occur. A critical gradient scale length of $a/L_{n_e} \approx 1.0$ was found to characterize the transition from flat impurity profiles of dominant anomalous transport to centrally peaked ones of dominant (neo)classical transport. The applicability of this critical scale length was found to be restricted to the region of peaked impurity density profiles (inside half radius). Therefore, another mechanism that introduces this radial dependency must be at play.

The previously presented data paints a grim picture of the impurity content in the assessed kind of discharge and thus the most commonly used path to high energy confinement in W7-X. The appearance of a transition from dominant anomalous to (neo)classical impurity transport at low neoclassical transport levels might, however, allow tailoring of the impurity transport properties via the latter. In contrast to the ion-root solutions with inward neoclassical impurity transport found in W7-X, geometries with electron-root solutions have been found [40, 41] which would lead to favorable outward impurity transport.

Besides such approaches relevant to future machines only, further probing the available parameter space of W7-X is essential. Additional parameters expected to affect the impurity transport, such as the magnetic field strength or plasma beta, might allow for NBI-based scenarios of high energy confinement without centrally peaked impurity density profiles. In addition, experiments being conducted in the current operational campaign (OP2.2), probe the dependence on the number of neutral beam sources. With changing power per particle facilitated by this variation, changes in impurity transport properties are anticipated. The discussion of the results of these investigations is subject to future works.

Data availability statement

The data cannot be made publicly available upon publication due to legal restrictions preventing unrestricted public distribution. The data that support the findings of this study are available upon reasonable request from the authors.

Acknowledgments

ORCID iDs

T Romba ⬤ https://orcid.org/0000-0002-2727-9385
S Bannmann ⬤ https://orcid.org/0000-0003-0772-9278
P Zs Poloskei ⬤ https://orcid.org/0000-0001-7781-5599
M Wappl ⬤ https://orcid.org/0000-0001-7847-8627

References

[1] Morita S *et al* 2011 *Plasma Sci. Technol.* **13** 290
[2] Nespoli F *et al* 2022 *Nat. Phys.* **18** 350
[3] Pütterich T 2005 Investigations of spectroscopic diagnostic of high-Z elements in fusion plasmas *PhD Thesis* Augsburg University
[4] Reiter D, Wolf G and Kever H 1990 *Nucl. Fusion* **30** 2141
[5] Freidberg J 2008 *Plasma Physics and Fusion Energy* (Cambridge University Press)
[6] Beidler C *et al* 2011 *Nucl. Fusion* **51** 076001
[7] Erckmann V *et al* (The W7-AS Team and The W7-X teams at IPP Garching, FZK Karlsruhe and IPF Stuttgart) 1997 *17th IEEE/NPSS Symp. Fusion Engineering (Cat. No. 97CH36131)* vol 1 (IEEE) pp 40–48
[8] Grulke O *et al* 2024 *Nucl. Fusion* **64** 112002
[9] Beidler C *et al* (The W7-X Team) 2021 *Nature* **596** 221
[10] Romba T *et al* (The W7-X Team) 2023 *Plasma Phys. Control. Fusion* **65** 075011
[11] Alcusón J *et al* (The W7-X Team) 2023 *Nucl. Fusion* **63** 094002
[12] Langenberg A *et al* (The W7-X Team) 2020 *Phys. Plasmas* **27** 052510
[13] García-Regaña J *et al* 2021 *J. Plasma Phys.* **87** 855870103
[14] Geiger B *et al* (The W7-X Team) 2019 *Nucl. Fusion* **59** 046009
[15] Yamada H *et al* 2005 *Nucl. Fusion* **45** 1684
[16] Baldzuhn J *et al* (The W7-X Team) 2020 *Plasma Phys. Control. Fusion* **62** 055012
[17] Lunsford R *et al* (The W7-X Team) 2021 *Phys. Plasmas* **28** 082506
[18] Romba T, Reimold F, Jaspers R, Ford O, Vanó L and Klinger T (The W7-X Team) 2023 *Nucl. Fusion* **63** 076023
[19] Zhang D *et al* (The W7-X Team) 2023 *Plasma Phys. Control. Fusion* **65** 105006
[20] Bannmann S *et al* (The W7-X Team) 2024 *Nucl. Fusion* **64** 106015
[21] Langenberg A *et al* (The W7-X Team) 2024 *Phys. Plasmas* **31** 052502
[22] Fonck R 1985 *Rev. Sci. Instrum.* **56** 885
[23] Ford O *et al* (The W7-X Team) 2020 *Rev. Sci. Instrum.* **91** 023507
[24] Swee C, Geiger B, Dux R, Kumar S, Castillo J, Bader A and Gerard M 2021 *Plasma Phys. Control. Fusion* **64** 015008

[25] Bannmann S *et al* (The W7-X Team) 2023 *J. Instrum.* **18** P10029

[26] Spanier A *et al* (The W7-X Team) 2021 *Fusion Eng. Des.* **163** 112115

[27] Beurskens M *et al* (The W7-X Team) 2021 *Nucl. Fusion* **61** 116072

[28] Bozhenkov S *et al* 2017 *J. Instrum.* **12** 10004

[29] García-Regaña J, Calvo I, Parra F and Thienpondt H 2024 *Phys. Rev. Lett.* **133** 105101

[30] Thienpondt H, García-Regaña J, Calvo I, Acton G and Barnes M 2024 *Nucl. Fusion* **65** 016062

[31] Goodman A, Xanthopoulos P, Plunk G, Smith H, Nührenberg C, Beidler C, Henneberg S, Roberg-Clark G, Drevlak M and Helander P 2024 *PRX Energy* **3** 023010

[32] Proll J, Plunk G, Faber B, Görler T, Helander P, McKinney I, Pueschel M, Smith H and Xanthopoulos P 2022 *J. Plasma Phys.* **88** 905880112

[33] Costello P and Plunk G 2025 *J. Plasma Phys.* **91** E12

[34] Landreman M, Choi J, Alves C, Balaprakash P, Churchill R, Conlin R and Roberg-Clark G 2025 arXiv:2502.11657

[35] Hirshman S, Shaing K, Van Rij W, Beasley C Jr and Crume E Jr 1986 *Phys. Fluids* **29** 2951

[36] Smith H 2022 NEOTRANSP (available at: https://gitlab.mpcdf.mpg.de/smithh/neotransp)

[37] Kappatou A, McDermott R, Pütterich T, Dux R, Geiger B, Jaspers R, Donné A, Viezzer E and Cavedon M (The ASDEX Upgrade Team) 2018 *Plasma Phys. Control. Fusion* **60** 055006

[38] Alcusón J, Xanthopoulos P, Plunk G, Helander P, Wilms F, Turkin Y, von Stechow A and Grulke O 2020 *Plasma Phys. Control. Fusion* **62** 035005

[39] Plunk G, Helander P, Xanthopoulos P and Connor J 2014 *Phys. Plasmas* **21** 032112

[40] Beidler C D, Drevlak M, Geiger J, Helander P, Smith H M and Turkin Y 2024 *Nucl. Fusion* **64** 126030

[41] Lee B, Lazerson S, Smith H, Beidler C and Pablant N 2024 arXiv:2406.04147